Acta Biomaterialia xxx (xxxx) xxx

Contents lists available at ScienceDirect

Acta Biomaterialia

journal homepage: www.elsevier.com/locate/actbio

Full length article

Elevated interstitial fluid pressure promotes spheroid growth and reduces CAR-T therapeutic efficacy in solid tumors

Pilar Alamán-Díez [a,1], Silvia Ferrer-Royo [a,1], Carmen Oñate Salafranca [b], Pablo Martín Compaired [a], Patricia Balsas [a], Julián Pardo [b,c,d], José Manuel García-Aznar [a,b,*], Alejandra González-Loyola [a,*,2]

[a] Multiscale in Mechanical and Biological Engineering (M2BE), Aragon Institute of Engineering Research (I3A), University of Zaragoza, Zaragoza, Spain
[b] Aragon Health Research Institute (IISA), Zaragoza, Spain
[c] Faculty of Medicine, University of Zaragoza., Zaragoza, Spain
[d] CIBER of Infectious diseases, IS Carlos III, Madrid, Spain

ARTICLE INFO

Keywords:
Pancreatic ductal adenocarcinoma (PDAC)
Tumor microenvironment (TME)
Interstitial fluid pressure (IFP)
CAR-T cells

ABSTRACT

Pancreatic ductal adenocarcinoma (PDAC) is among the deadliest solid tumors and is characterized by aggressive progression, a dense tumor microenvironment (TME), and resistance to conventional therapies. Among the barriers to effective treatments, the presence of elevated interstitial fluid pressure (IFP) may be important for drug penetration and immune cell infiltration. In this work, we present an innovative 3D microfluidic PDAC-on-a-chip that allows the application of IFP in a cell chamber to simulate the TME and evaluate the therapeutic efficacy of CAR-T cells engineered against the receptor EGFR expressed in tumor cells. Elevated IFP was associated with increased tumor spheroid growth, reduced caspase activation and decreased actin remodeling, indicating enhanced tumor resistance. CAR-T cells effectively targeted and eliminated tumor cells in 2D and 3D coculture models under normal pressure conditions. However, under high IFP, CAR-T-mediated cytotoxicity was impaired, indicating that some of the low efficacy of CAR-T cell therapy against solid tumors might be derived from IFP. These results highlight the importance of the mechanoenvironment in limiting the efficacy of current immunotherapies. Our model, which incorporates an IFP component, serves as a realistic preclinical platform for testing antitumor therapies in solid tumors.

Statement of Significance

In this work, we present an innovative 3D pancreatic tumor-on-a-chip model that incorporates interstitial fluid pressure (IFP), which is a key mechanical component of solid tumors. Using this platform, we discovered that IFP enhances tumor proliferation whilst diminishing immunotherapy efficacy. This indicates the important role of mechanical pressure in limiting immune cell function in solid tumors. Our model is a valuable preclinical platform for investigating the efficacy of anti-tumor therapies and supports the development of strategies to overcome mechanical resistance and enhance therapy efficacy in solid tumors, such as pancreatic cancer.

1. Introduction

Pancreatic cancer is among the deadliest and fastest-killing cancers. It has a five-year survival rate of only 9% and represents the seventh leading cause of cancer-related deaths worldwide [1]. Among all types of pancreatic cancer, the most common is pancreatic ductal adenocarcinoma (PDAC), which affects the ducts where pancreatic juice is released. PDAC has no cure and is expected to be the second leading cause of cancer-related deaths by 2030 [2]. The high mortality rates associated with this malignancy are due mainly to late diagnosis and tumor microenvironment (TME) characteristics [3,4], which increase the resistance offered by the tumor to all kinds of therapies [5,6].

The PDAC TME is characterized by high heterogeneity of cellular and noncellular components, a dense fibrotic stroma due to the presence of numerous cancer-associated fibroblasts (CAFs) and an extracellular matrix (ECM) rich in fibrous proteins, especially collagen type I [3]. The stiff and complex PDAC ECM constitutes a physical

* Corresponding authors.
E-mail addresses: jmgaraz@unizar.es (J.M. García-Aznar), agonzalezlo@iisaragon.es (A. González-Loyola).
[1] These authors contributed equally to this work.
[2] Current address: Aragon Health Research Institute, (IISA) Zaragoza, Spain; Aragonese Agency Foundation for Research and Development (ARAID), Zaragoza, Spain.

https://doi.org/10.1016/j.actbio.2026.01.050
Received 1 September 2025; Received in revised form 16 January 2026; Accepted 27 January 2026
Available online 28 January 2026

barrier for chemotherapy drugs and is a source of residual solid stresses, which can impact tumor behavior [7]. These residual stresses supported by the ECM as well as the sparse and permeable blood vessels and the lack of functional lymphatic vessels have been postulated as the cause of the elevated interstitial fluid pressure (IFP) found in PDAC [8]. Moreover, very high IFP values prompt vascular collapse and intratumoral hypoxia, which increase tumor resistance to chemotherapy and immunotherapy [9,10]. In addition, in this type of cancer, the abundance of hyaluronan secreted by activated CAFs has been reported to increase the IFP [11,12].

External mechanical forces are known to influence tumor growth and behavior. To better understand these effects, the latest mechanobiological models have been proposed to integrate the biophysical complexity of the TME to predict treatment outcomes [13]. For instance, when tumor spheroids are embedded in nonporous or stiff agarose matrices, their expansion is physically constrained by compressive stresses, leading to growth inhibition [14–16]. Similarly, mechanical stress has been shown to slow or arrest proliferation in multicellular aggregates [17]. However, the underlying mechanisms depend on the nature of the surrounding material. Thus, in nonporous environments, physical confinement is predominant, whereas in porous matrices, such as collagen hydrogels, cellular growth may be modulated by interstitial flow, fluid pressure, mechanical properties or solid stress transmission [18,19].

The mechanical properties of hydrogels are especially relevant in the context of pancreatic tumors, where elevated IFP levels have been reported. While normal IFP in a healthy pancreas remains close to atmospheric levels, studies have shown increased IFP values in PDAC patients to be approximately 20 mmHg [20]. In addition, IFP values ranging from 13 to 45 mmHg were measured in tumors generated in mice from the established PDAC cell line PANC-1 [21]. Moreover, Provenzano et al. used genetically engineered mouse models of PDAC and obtained IFP values ranging from 75 to 130 mmHg [11]. Although the relevance of high IFP in PDAC is widely accepted, to the best of our knowledge, no assays have determined the effects of IFP on pancreatic tumor cells at the morphological, structural and growth levels.

Thus, we developed a unique PDAC-on-a-chip model using human pancreatic tumor spheroids grown in a microfluidic device under relevant IFP values. External pressure was applied over the cultures through a printed system based on the one developed by Shang et al. [22]. This system enabled the application of a maximum IFP of 29.3 mmHg to microfluidic 3D cultures of two established PDAC cell lines (PANC-1 and BxPC-3) grown in collagen type I hydrogels to mimic the PDAC TME.

Over the past decade, multiple strategies targeting CAFs or the ECM in PDAC have been attempted with no success [23–25]. This scenario highlights the urgent need to develop innovative experimental therapies to inhibit PDAC progression. In this context, different approaches based on controlling and enhancing the response of the immune system are being studied. One of these strategies is CAR-T cell therapy, a new antitumor treatment in which patient-derived T cells are genetically engineered to express a chimeric antigen receptor (CAR) that allows recognition and specific binding to tumor cells [26,27].

Although CAR-T cell immunotherapy has proven to be a successful tool for treating hematological malignancies such as B-cell acute lymphoblastic leukemia, large B-cell lymphoma and multiple myeloma [28], solid tumors remain a challenge [29–31]. To date, no CAR-T cell therapies have been approved for the treatment of solid tumors; however, they are being studied as promising therapies for PDAC [32–34]. In fact, a systematic review of clinical trials of CAR-T cells revealed that until 2022, 42 international trials targeting pancreatic cancer were registered on ClinicalTrials.gov [35].

In this study, we used CAR-T cells expressing a second-generation CAR that is selectively activated by several members of the ErbB family, including the epidermal growth factor receptor (EGFR) [36]. The upregulation of EGFR in various solid tumors, including pancreatic cancer, overactivates pro-oncogenic signaling pathways such as the JAK/STAT, RAF/MEK/ERK and PI3K/AKT/mTOR pathways [37]. This CAR is engineered to coexpress a panErbB-specific CAR called T1E28ζ and an IL-4-responsive chimeric cytokine receptor, 4$\alpha\beta$, which allows IL-4-mediated proliferation. We investigated the effectiveness of CAR-T cell therapy in our innovative platform. Our results revealed that IFP not only promoted tumor growth but also significantly limited CAR-T cell efficacy in our human PDAC *in vitro* model. This is the first study in which such a dynamic and physiologically relevant system has been employed to assess EGFR-targeting CAR-T cell behavior in the context of pancreatic cancer modeling under IFP. This platform allows us to better understand the role of IFP in solid tumor growth and behavior and may serve as a valuable preclinical tool to better understand CAR-T cell performance in solid tumors and to guide the design of future and effective immunotherapies.

2. Materials and methods

2.1. Tumor cell culture

In this study, two well-established PDAC cell lines were used: PANC-1 and BxPC-3. Both cell lines were cultured in Dulbecco's modified Eagle's medium (DMEM; Gibco) supplemented with 10% fetal bovine serum (FBS; Sigma-Aldrich) and 1% streptomycin/penicillin (Pen/Strep; Gibco). These cells were obtained from the ATCC repository and used until maximum passage 20. Once expanded, the tumor cells were grown as spheres by incubation in T-25 flasks coated with poly(2-hydroxyethyl methacrylate) (pHEMA; Sigma-Aldrich) to prevent attachment to the flask surface, as previously described [38]. The cells were maintained in DMEM/Nutrient Mixture F-12 (DMEM/F-12; Gibco) supplemented with 2% B-27 supplement (Gibco), 0.02% recombinant human basic fibroblast growth factor (bFGF; Gibco) and 1% Pen/Strep. After 3 days of growth as spheres, the cells were disaggregated, counted, and subsequently incorporated as single cells into the collagen hydrogel mixture, the preparation of which is described in Section 2.6.

2.2. Primary human T cells: culture and transduction to CAR-T cells

Human peripheral blood mononuclear cells (PBMCs) were obtained from the Biobank of the Aragon Health System (National Registry of Biobanks B. B.000873) (PT23/00146) and integrated into the ISCIII Biobanks and Biomodels Platform. All procedures were conducted in accordance with standard operating protocols and with appropriate approval from the Ethics and Scientific Committees. The starting material used throughout the study consisted of leukopaks from healthy donors. Cells were isolated by Ficoll–Paque density gradient centrifugation and either used fresh or cryopreserved. Activation was performed with anti-CD3 and anti-CD28 antibodies (BD Pharmingen) in RPMI 1640 medium (Pan Biotech) supplemented with 10% FBS Xtra (Capricorn Sci.), penicillin/streptomycin (Sigma-Aldrich), GlutaMAX (Gibco), nonessential amino acids (Sigma-Aldrich), and 1 mM sodium pyruvate (Sigma-Aldrich). After 24 h, IL-7 and IL-15 were added (10 ng/mL), and at 48 h, the cells were collected for lentiviral transduction. After transduction, the cultures were maintained with IL-4 (30 ng/mL), which was replenished every 48 h. Transduction was performed at an MOI of 10, and efficiency was assessed by flow cytometry on Days 4–5. Fig. 1 shows the fabrication and functionality of CAR-T cells.

2.3. Construction and generation of lentiviral vectors

Starting from the original plasmid SFG T4 [36], provided by John Maher (King's College Hospital, London), the CAR construct (T1E28z) together with the 4$\alpha\beta$ chimeric cytokine receptor was cloned and inserted into the clinical-grade pCCL backbone. The insert included a T2 A self-cleaving peptide followed by eGFP for reporter expression.

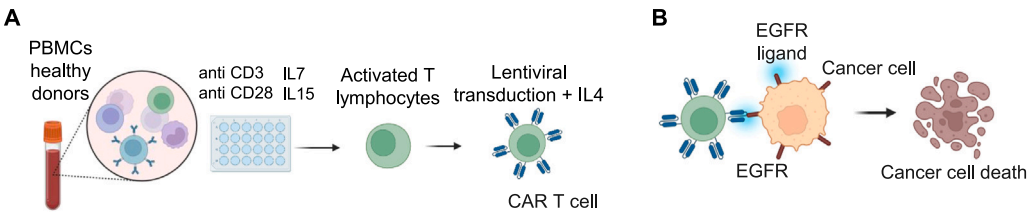

Fig. 1. CAR-T cells were generated from PBMCs from healthy donors and engineered to express a chimeric antigen receptor (CAR) targeting ErbB family members such as EGFR (A), enabling the specific recognition and killing of EGFR-positive cells, such as PANC-1 cells (B).

A control lentivirus containing only eGFP in the pCCL vector was also generated. Third-generation lentiviruses were produced in 293T cells using polyethylenimine (PEI) transfection, together with the packaging plasmids pMDLg/pRRE, pRSV-Rev, and VSV-G as the envelope plasmid. Viral supernatants were harvested 72 h post-transfection, clarified by filtration and centrifugation, and concentrated either by ultracentrifugation or with Lenti-X Concentrator (Takara). Preparations were stored at - 80°C.

2.4. Analysis of 2D cell seeding and live/dead cells

To measure the cytotoxicity mediated by lymphocytes transduced to express the T4 CAR, an Incucyte® live-cell imaging and analysis system was used. A total of 10,000 target cells per well, previously labeled with eFluor 670, were seeded in a 96-well culture plate. After waiting for at least 5 h to allow proper adherence to the surface, lymphocytes were added at different effector:target ratios. The lymphocytes were added on Day 5 after the start of transduction. At the beginning of the coculture, the volume per well was 200 µL. The loss of the NIR event count was measured using Incucyte® at 24 h after the start of coculture. The results were normalized to the condition with nontransduced lymphocytes and to the number of target cells at time 0 of the coculture.

2.5. Microfluidic device fabrication

Microfluidic devices were fabricated in poly(dimethysiloxane) (PDMS) by soft lithography, following the methodology described by Shin et al. [39]. The geometry consisted of one single culture chamber connected to two reservoir channels for culture hydration. The inner geometry of the microfluidic device is shown in Fig. 2-A. After curing, the PDMS wafers were trimmed and perforated to create individual platforms. PDMS devices were sterilized before being bonded to 35 mm glass bottom dishes (Ibidi) by plasma treatment (PDC-32G Basic Plasma Cleaner; Harrick Plasma) under vacuum conditions. A 2 mg/mL polydopamine (PDA; Sigma-Aldrich) solution was injected into the geometry to improve surface-matrix attachment, restoring hydrophobicity [40].

2.6. Collagen hydrogel fabrication and injection in the microfluidic platform

Collagen hydrogels, with a final collagen concentration of 4 mg/mL, were prepared by diluting collagen type I solution (rat tail, stock 10.35 mg/mL; Corning) in DMEM-F12, 10× Dulbecco's phosphate-buffered saline (DPBS) and 0.5 M NaOH (both from Sigma-Aldrich) to adjust the pH to 7.4 [27,41,42]. The cellular component was incorporated into the collagen mixture prior to gelation. Specifically, for the monoculture PDAC models, PANC-1 or BxPC-3 cells were suspended at a concentration of $1*10^6$ cells/mL in culture medium and added to the collagen solution at a volume ratio of 1:5 (20% of the final mixture). After gently pipetting the solution into the culture chamber, it was polymerized for 20 min in a humid chamber at 37 °C. The culture was then hydrated through the medium ports with DMEM-F12. This medium was exchanged every 48 h to ensure nutrient delivery to the cultures.

2.7. 3D printed system for IFP application

To simulate the IFP experienced by cancer cells within a tumor environment [43,44], we developed a custom 3D-printed system modeled following the design proposed by Shang et al. [22]. This system featured a scaffold-like structure that supported four syringes, which were connected to the medium reservoirs of the microfluidic devices via silicone tubing. Both the syringes and the tubing were filled with cell culture medium. In our set up, IFP stability derives from the hydrostatic equilibrium condition and the constant height of the fluid columns confirmed daily from Day 1 to Day 5 after IFP induction. The applied IFP was calculated using the hydrostatic pressure equation:

$$IFP = h \cdot \rho \cdot g \tag{1}$$

where h is the height of the fluid column, ρ is the density of the liquid, and g is the gravitational acceleration.

The syringe holder assembly consisted of a base to secure the microfluidic device, four modular columns that allowed an adjustable height, two dowels for positioning, and a syringe holder to keep the syringe in place during operation. The base ensured the stability of the device, whereas modular columns provided flexible configurations. Fixed parts (base and columns) were connected through threaded joints, whereas movable elements (dowels and syringe holder) were fitted with mating holes to allow precise positioning and stability (Fig. 2-B). Additional information regarding the fabrication and sterilization procedures is provided in the Supplementary Material, along with a rendering of the designed geometry (Fig. S1). Besides, a complete view of the stepwise IFP application set up is shown in Fig S11. Moreover, to validate the imposed IFP, we performed computational fluid dynamics simulations in OpenFOAM to reproduce the device geometry and fluid height differences, which yielded pressure values in agreement with the theoretical calculations (Fig S1-C).

2.8. Tumor cell and immune cell culture

For the 2D and 3D coculture experiments, a 8:1 lymphocyte:PANC-1/BxPC-3 ratio was used. In the 3D experiments, 10% of the total hydrogel volume was composed of PDAC cells (at $1 \cdot 10^6$ cells/mL), while an additional 10% was made up of lymphocytes, either CAR-T cells or control T cells, at a concentration of $8 \cdot 10^6$ cells/mL, resulting in final embedded cell concentrations of $1 \cdot 10^5$ PANC-1/BxPC-3 cells/mL and $8 \cdot 10^5$ lymphocytes/mL within the gel. Collagen I polymerization was conducted following the procedure detailed in Section 2.6.

2.9. T and CAR-T cell infiltration inside the collagen hydrogel along a chemoattractant gradient

To assess immune cell infiltration in the hydrogel independent of tumor-related factors, a hydrogel mixture without cells was injected into the microfluidic devices and incubated overnight to allow complete gelation. The following day, the cytokine C-X-C motif chemokine 12 (CXCL12), a well-known chemoattractant for immune cells that is frequently upregulated in the TME [27,45], was introduced into the system. To mimic this condition, CXCL12 (1:500 dilution) was added

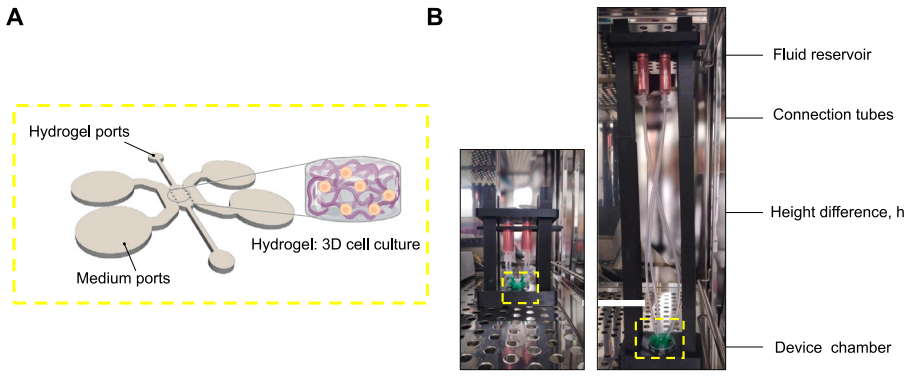

Fig. 2. (A) Schematic of the microfluidic device: geometry used for all experiments to enable 3D cell culture. (B) Front view of the 3D-printed prototypes with the 10 cm (7.3 mmHg) and 40 cm height sets (29.3 mmHg).

through the lateral channel of the device and incubated for 5 h. Subsequently, $3 \cdot 10^5$ cells/mL (control T and CAR-T cells) were introduced through the opposite channel, amounting to 80 μL (≈ 24.000 cells), and their visualization under the microscope was initiated. A schematic representation of the experimental design is shown in Fig. S7. Over the following 15 h, images of the entire chamber were acquired using an Axio Observer 7 (Zeiss) to track the infiltration of control T cells and CAR-T cells into the hydrogel. Cells penetrating the hydrogel were counted using ImageJ.

2.10. Microscopy, immunostaining and image analysis

Bright-field images of the central chamber of each microfluidic device were acquired on Day 1 after seeding and on Day 6, after the structures were dismantled. Images were acquired using an optical microscope (Leica DM IL LED – Pylon Viewer software). The area of the spheroids was quantified at both time points using FIJI. Thus, the spheroid growth ratio (SGR) was calculated as the ratio between the spheroid area on Day 6 of culture and its corresponding area on Day 1.

At the end of the experiment, the samples were fixed with 4% paraformaldehyde (Sigma-Aldrich), permeabilized using 0.1% (v/v) Triton X-100 (Calbiochem) and blocked with 5% (w/v) bovine serum albumin (BSA, VWR). For immunostaining, the cells were incubated overnight at 4 °C with the appropriate primary antibodies: mouse anti-Ki-67 (1:200; Santa Cruz Biotechnology), rabbit anti-EGFR (1:100; Thermo Fisher Scientific), or rabbit anti-cleaved caspase-3 (1:300; Cell Signaling Technology). The following day, the samples were rinsed and incubated at room temperature with DAPI (1:100; Invitrogen), TRITC-conjugated phalloidin (1:200; ChemCruz), and the appropriate secondary antibodies, namely, goat anti-mouse IgG, goat anti-rabbit IgG conjugated to Alexa Fluor™ 647 or Alexa Fluor™ 555 (1:200; Thermo Fisher Scientific).

Fluorescence imaging was performed using an Axio Observer 7 inverted fluorescence microscope (Zeiss). The images were analyzed using FIJI. Multichannel images were split into individual channels and subsequently analyzed as follows: for proliferation analysis, the proportion of proliferative spheroids (defined by the presence of at least one Ki-67-positive cell) was calculated. To study cytoskeletal features using phalloidin-TRITC, the mean intensity values of F-actin per spheroid were determined under control and IFP conditions. To assess EGFR expression in PDAC cells, the mean fluorescence intensity in the designated channel was quantified for each spheroid and compared across experimental conditions. Finally, to detect and quantify apoptotic cell death, the number of caspase-3-positive spheroids in the absence and presence of CAR-T cells was calculated. To study spheroid permeability to low molecules, 4kDa FITC-dextran was added 1 day after PANC-1-embedded spheroids were seeded in 4 mg/ml collagen I hydrogel. A z-stack video was obtained 1 h after the addition of dextran.

To assess potential alterations in collagen fiber organization caused by prolonged IFP, second-harmonic generation (SHG) multiphoton microscopy (Stellaris-Dive; Leica) was employed. This technique allows the label-free visualization of collagen fibers by exploiting their nonlinear optical properties. After 5 days of incubation, the samples were imaged under two conditions: control (no applied pressure) and high IFP (29.3 mmHg). For each condition, three representative samples were imaged. Structural arrangement and collagen fiber alignment were qualitatively evaluated through the SHG signal in acellular hydrogels.

2.11. Flow cytometry

PANC-1 and CAR-T cells were seeded without a hydrogel in the central chamber of the device. IFP was induced as previously described in methods Section 2.7. Five days after IFP induction, the cells were recovered and centrifuged at 1500 rpm for 5 min. The cells were then stained with conjugated antibodies at 1/100 in PBS+2% FBS (blocking buffer) for 20 min on ice, centrifuged and resuspended in 100 μl of blocking buffer. The antibodies used were PD-1 APC, TIM-3 PE-Cy7, LAG-3 APC, 7-AAD (viability) and CD45 BV421 (Miltenyi Biotec). Samples were acquired on a MACSQuant 10 (Miltenyi Biotec) cytometer with compensation using single-cell staining and analyzed with Kaluza software. For flow cytometry analysis, the presence of CAR-T cells was detected as the presence of GFP+ cells. The gating strategies are presented in Fig. S10.

2.12. Enzyme-linked immunosorbent assay (ELISA) analysis

Human IFN-γ secretion from a coculture of PANC-1 and CAR-T/control T cells was quantified using a commercially available ELISA kit (BD OptEIA; BD Biosciencies), following the manufacturer's instructions. ELISA was performed with the supernatant from microfluidic cultures of PANC-1 and CAR-T/control T cells that were seeded without hydrogel in the central chamber of the device for 5 days of coculture under either no pressure or elevated IFP. All the conditions were assayed in technical duplicates and derived from at least three independent microfluidic devices per condition.

2.13. Statistical analysis

GraphPad Prism 8.0.2 software was used for statistical analysis and graphical representation of the microscopy-derived data. The number of measured samples is indicated in the figure legends. For all the datasets, normality tests were performed. Afterward, the most appropriate statistical tests were selected and applied to each dataset. For experiments in which a single independent variable was compared between two groups, unpaired t tests or Mann–Whitney tests were performed. For experiments in which a single independent variable was compared among multiple groups, one-way ANOVA followed by

the post hoc Tukey–Kramer test or Kruskal–Wallis test and then by a post hoc Dunn test was performed. Scattered dot plot data are shown as medians with ranges or means with SD. Statistical significance is indicated by p values (ns; $p > 0.05$; *, $p \leq 0.05$; **, $p \leq 0.01$; ***, $p \leq 0.001$; ****, $p \leq 0.0001$) and is presented in the figures.

3. Results

3.1. IFP enhances PDAC growth

PANC-1 spheroids were initially grown in collagen I hydrogels at two different concentrations, achieving larger spheroids at 4 mg/mL than at 6 mg/mL collagen I matrix (Fig. S3). Thus, the 4 mg/mL collagen hydrogel was used for the subsequent experiments. When low-molecular-weight FITC–dextran was added to the device, the spheroids appeared impermeable to the dye (Video S1). These observations suggested that the spheroids formed a compact structure that regulated the diffusion within the device, thereby limiting the penetration of small molecules into the tumor mass.

Prior to evaluating the biological outcomes under any pressure, we assessed whether the application of IFP could induce any relevant structural changes in the collagen matrix. Hence, acellular hydrogels were incubated under high-pressure conditions and imaged via multi-photon microscopy to determine the effect of IFP on collagen fibers. Macroscopic inspection and high-resolution imaging suggested that the hydrogel architecture remained largely preserved, with no evident alterations observed (Fig. S2).

PANC-1 and BxPC-3 spheroids were seeded in one channel microfluidic devices, and their growth was followed for 6 days (Fig. 3-A). Afterward, using our new 3D-printed system described above (Fig. S1 and S11), PANC-1 spheroids were continuously subjected to IFP values of 7.3 mmHg and 29.3 mmHg from Day 1 to Day 6 after cell seeding (Fig. 3-B).

Compared with control spheroids, PANC-1 spheroids exposed to elevated IFP exhibited significantly higher growth ratios (Fig. 3-C). Samples at 29.3 mmHg achieved the highest mean SGR (3.131 ± 0.064) versus 2.941 ± 0.073 at 7.3 mmHg and 2.786 ± 0.054 for controls ($P \leq 0.0032$ vs. 7.3 mmHg; $P \leq 0.0001$ vs. control). Analysis of SGR distributions further revealed that while approximately 31.7% of control spheroids were within the lowest category (SGR < 2), this percentage decreased under pressure (27.5% at 7.3 mmHg and 20.1% at 29.3 mmHg). Conversely, the percentage of spheroids with the highest SGR (>4) increased from 13.6% in the controls to 19.5% and 25% in the 7.3 mmHg and 29.3 mmHg conditions, respectively.

Throughout the experiments, PDAC cultures were initiated using dissociated preformed spheroids, which were disaggregated into single cells prior to being seeded inside the hydrogel. This approach was selected to retain the phenotypic and transcriptional adaptations that tumor cells acquire during initial spheroid formation, a phenomenon often referred to as "3D culture memory" [46]. Next, to analyze whether IFP had the same effect on advanced tumors, preformed spheroids were directly introduced into the devices and subjected to IFP. Under these conditions, no differences were observed between the IFP and control conditions, suggesting that its influence might be more relevant during earlier stages of tumor development than other mechanisms, such as aggregation dynamics and outer-layer barriers (Fig. 3-D). Therefore, all subsequent experiments were conducted using single-cell suspensions derived from preformed spheroids to ensure consistent spheroid formation and responsiveness to IFP modulation.

In the case of the BxPC-3 line, spheroid growth was comparable at both 4 and 6 mg/mL collagen (Fig. S4-A and B). As observed in PANC-1 cells, BxPC-3 spheroids exposed to elevated IFP had a significantly greater SGR compared with control spheroids ($P < 0.0001$), with mean values of 4.016 ± 0.109 at 29.3 mmHg, 3.916 ± 0.118 at 7.3 mmHg, and 3.210 ± 0.088 under control conditions (Fig. S4-C). Analysis of SGR distributions revealed that while 27.9% of control spheroids reached values above 4, this fraction increased to 45.9% and 41.6% under 7.3 mmHg and 29.3 mmHg, respectively. These results indicated that, similar to PANC-1 cells, BxPC-3 spheroids exhibited enhanced growth when cultured under IFP.

3.2. IFP induces changes in proliferation and cytoskeletal dynamics

Cell proliferation and cytoskeletal organization were evaluated in PANC-1 spheroids subjected to low and high IFP conditions. The ratio of proliferative spheroids between control and IFP conditions (defined by the presence of at least one Ki67-positive cell) was analyzed. Compared with control spheroids, PANC-1 spheroids subjected to IFP tended to have an increased proliferation rate (Fig. 4-A).

Conversely, quantification of phalloidin fluorescence intensity revealed a significant decrease in F-actin levels with increasing IFP. Spheroids exposed to 29.3 mmHg exhibited the lowest mean intensity (1452 ± 59.33), followed by those at 7.3 mmHg (1656 ± 44.46) and the controls (1760 ± 48.55) (Fig. 4-B), suggesting a potential pressure-induced alteration in cytoskeletal organization. These changes in F-actin levels might be related to the mechanical and functional behavior of tumor spheroids, since high actin levels have been associated with increased migration and invasive capacity in 3D environments [42]. Therefore, the observed reduction in F-actin upon high IFP could imply a reduction in the migration capacity of these spheroids, suggesting that IFP altered their mechanical phenotype.

3.3. CAR-T cells effectively targeted PDAC cells in 2D and 3D coculture models under IFP-free conditions

In this study, we utilized a CAR (referred to as T1E28z by Davies et al. [36]) that is specifically activated by all ErbB1-based homodimers and heterodimers as well as the ErbB2/3 heterodimer. Notably, the overproduction of ErbB1 and/or ErbB2 plays a role in numerous carcinomas, including those affecting the pancreas [47]. Additionally, alongside the CAR, the IL-4 chimeric receptor ($4\alpha\beta$) was implemented. The ectopically expressed IL-4Rα/IL-2Rβ is connected intracellularly to IL-2/IL-15R, which governs T-cell activation and proliferation, suggesting that IL-4 (interleukin-4) may serve as a specific stimulus to initiate CAR-T cell proliferation and activation.

Different experimental approaches have been employed to evaluate the cytotoxic potential of CAR-T cell therapy in PDAC, and the efficacy of CAR-T-cell therapy has been compared in 2D cultures and 3D microfluidic models. First, the cytotoxic potential of CAR-T cells targeting EGFR was investigated in a 2D coculture, which minimized the influence of a three-dimensional architecture and focused only on cellular interactions in a simplified environment (Fig. 5-A). Second, 3D coculture experiments were conducted to evaluate CAR-T-cell performance within a more physiologically relevant microenvironment. CAR-T efficacy was assessed by measuring the percentage of live cells (Fig. 5-A) and through live imaging (Fig. 5-B) and morphological analysis (Fig. 5-C).

In 2D coculture experiments, CAR-T cells demonstrated robust cytotoxic activity, eliminating more than half of PANC-1 tumor cells within 24 h. In contrast, control T cells exhibited cytotoxicity levels comparable to those of the untreated cultures, indicating minimal or no tumor cell killing capacity (Fig. 5-A and S5). These results highlighted the specificity and potential of CAR-T cells in targeting EGFR-positive pancreatic cancer cells under simplified 2D conditions, where the absence of a complex architecture allows direct cell-to-cell interactions.

Moreover, CAR-T cells could recognize, target, and induce tumor cell death in a 3D culture environment. This cytotoxic activity is clearly illustrated in Fig. 5–B,C and Supplementary Video S5, where CAR-T cells interacted with PANC-1 tumor cells within the first 24 h of culture. After five days of coculture, the number of viable PANC-1 and BxPC-3

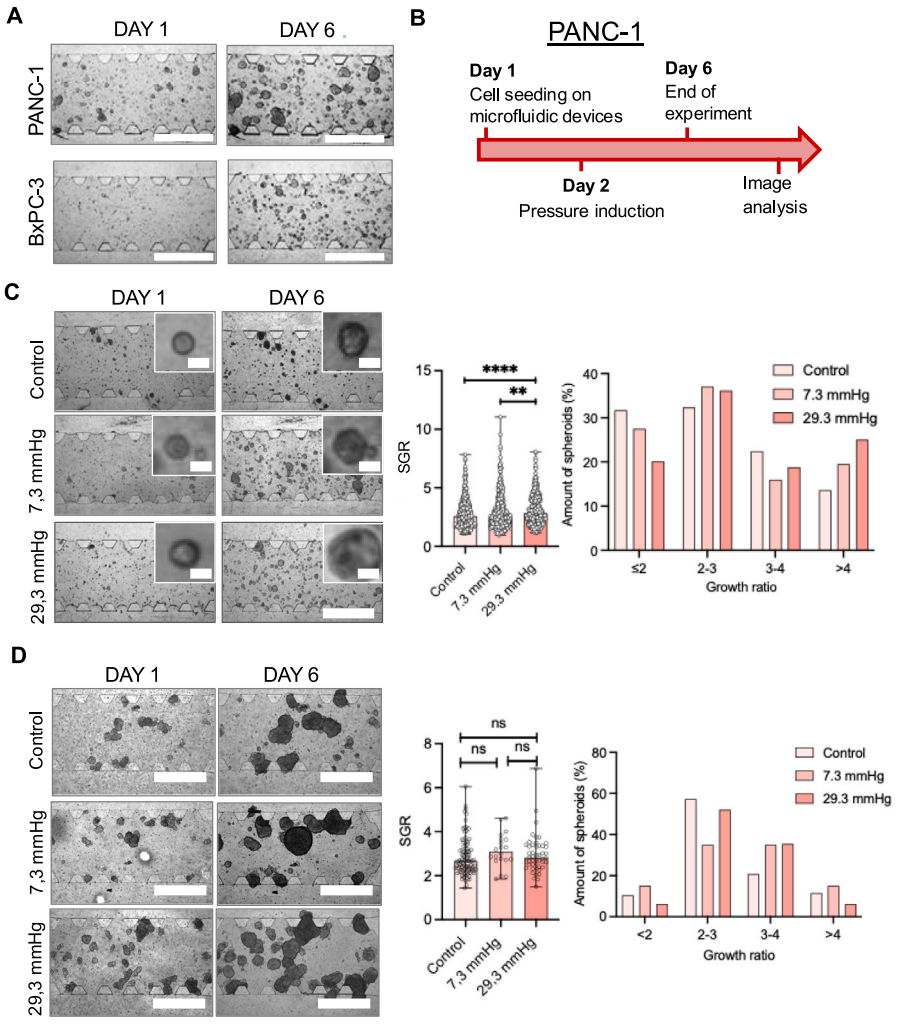

Fig. 3. Interstitial fluid pressure enhances pancreatic tumor growth: (A) Representative bright-field microscopy images of the central chamber of the microfluidic device cultured with PANC-1 or BxPC-3 cells at 4 mg/mL collagen on day 1 and 6 after seeding. Scale bar: 1 mm. (B) Workflow of the IFP experiments. (C) Representative PANC-1 cultures at the beginning and end of the experiment subjected to none, low, and high-pressure conditions. Samples were seeded from single cells. All the conditions were analyzed in terms of the SGR and spheroid count (n = 8–10 devices/condition). Scale bars, 1 mm and 25 μm. One-way ANOVA test was performed. ns: not significant, ** $p \leq 0.01$ and **** $p \leq 0.0001$. (D) IFP does not affect the growth of preformed spheroids. Quantification of preformed spheroids subjected to IFP (n = 2–6 devices/condition). Scale bar, 1 mm. One-way ANOVA test was performed. ns: not significant when comparing all conditions.

spheroids clearly decreased under CAR-T conditions (Fig. 5-C, Fig. S6-D). In the 3D coculture model, cellular damage can also be qualitatively evidenced by the loss of the initial spherical morphology of tumor cells, which transitioned into a collapsed and irregular structure, consistent with the morphological features of early apoptosis or necrosis [48]. In contrast, the results of the control T cells shown in Fig. 5-C and Video S4 demonstrated no such cytotoxic effect, with tumor cells retaining their typical morphology. Similar results were observed under both 2D and 3D conditions with BxPC-3 spheroids (Fig. S5, S6).

3.4. IFP attenuates CAR-T cell antitumor efficacy

To replicate the *in vivo* scenario in which CAR-T cells migrate from the vasculature into the tumor, CAR-T/control T cells were added through the lateral channels of the devices after the tumor cells were seeded in the central chamber. This setup allowed us to evaluate the potential cytotoxic activity of immune cells upon infiltration into the TME. In addition, IFP was applied under these conditions.

Images of whole chamber devices allowed us to visualize control T cells and CAR-T cells that were GFP tagged and infiltrated into the hydrogel where the tumor spheroids were embedded. Under IFP, CAR-T cells were frequently dispersed throughout the hydrogel matrix rather than clustering around tumor spheroids (Fig. 6-A). Moreover, the distance from lymphocytes to PANC-1 spheroids significantly increased under IFP conditions (Fig. 6-A). Both results suggested impaired tumor targeting and limited engagement with cancer cells. Compared with those in the IFP-free condition P_0, the number of spheroids and the SGR in the control and CAR-T conditions in IFP tended to increase. In P_0 condition, compared with that in the control T cell condition, the tumor spheroid area in the CAR-T condition was diminished. However, when IFP was applied, this difference was no longer observed (Fig. 6-B,C), indicating that CAR-T cells were less effective upon IFP. In contrast, no significant differences were observed in the control T condition, indicating that the effect was specific to CAR-T cell mediated cytotoxicity.

In addition to spheroid size, caspase 3 staining was quantified as an indicator of cell death. As shown in Fig. 6-C, the same trend was observed: compared with those treated with IFP, PANC-1 spheroids under P_0 cocultured with CAR-T cells exhibited higher caspase activity. These findings further supported the notion that elevated pressure impaired CAR-T mediated tumor cell death. One hypothesis that may explain this effect is that elevated IFP may alter CAR-T cell infiltration, reduce

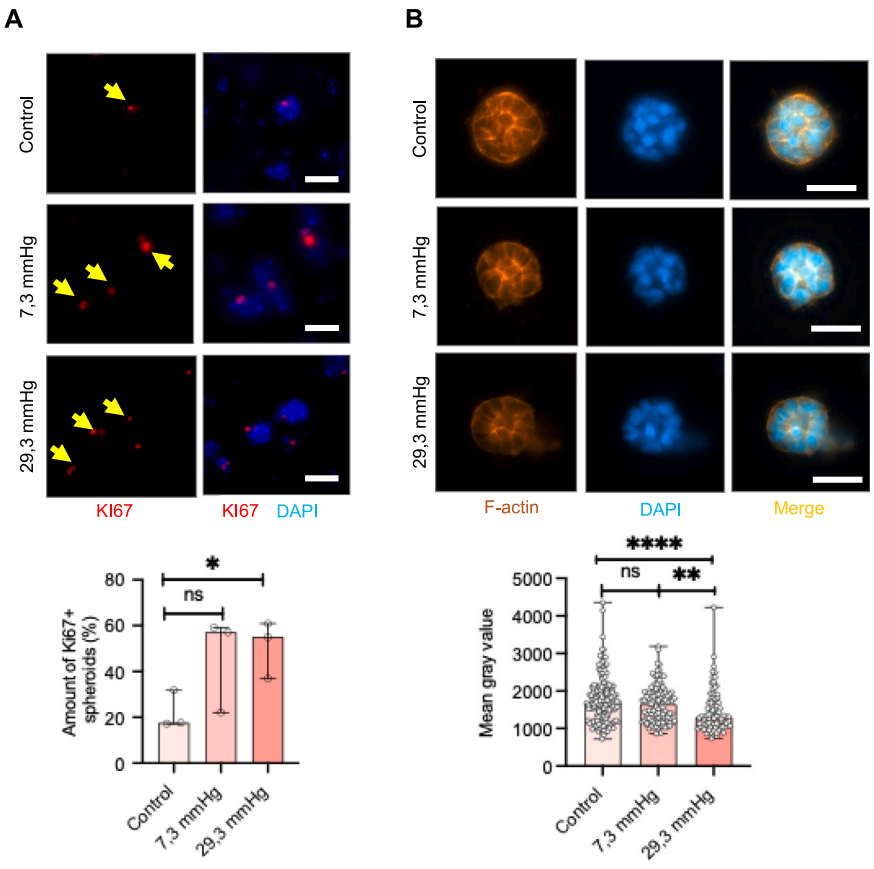

Fig. 4. PANC-1 spheroids changes in proliferation and cytoskeleton upon IFP condition. (A) Representative fluorescence microscopy images and quantification of Ki-67 expression (red staining) in samples subjected to different pressure conditions. Nuclei are stained with DAPI (blue). Scale bar, 200 μm. One-way ANOVA test was performed. ns: not significant and * $p \leq 0.05$. (B) Visualization and quantification of F-actin: Representative spheroids from each condition showing F-actin filaments (orange), nuclei (blue), and merged images revealing the overall spheroid structure. Scale bar, 50 μm. Quantification of F-actin intensity was performed to assess cytoskeletal organization under varying interstitial fluid pressures. $n = 3$ devices/condition. One-way ANOVA test was performed. ns: not significant, ** $p \leq 0.01$ and **** $p \leq 0.0001$. (For interpretation of the references to color in this figure legend, the reader is referred to the web version of this article.)

CAR-T cell motility, or disrupt receptor–ligand interactions essential for target recognition and killing.

Hence, we first analyzed the infiltration capacity of the CAR-T vs. control T cells. In this setup, a CXCL12 chemotactic gradient, which is commonly associated with T-cell recruitment in the TME [27,45], was applied across the collagen hydrogel without tumor cells (Fig. S7-A). This approach allowed us to assess the migratory capacity of CAR-T cells and control T cells under identical conditions. In the Supplementary Material, microscopy videos of representative infiltration experiments are shown (Videos S2 and S3). Although overall immune cell infiltration into the collagen hydrogel was limited (≈1% of cells infiltrated), not significant differences in infiltration capacity were observed between CAR-T cells and control T cells (Fig. S7-B). Therefore, the reduced CAR-T cell efficacy could nor be attributed to impaired infiltration into the TME.

Then, two alternative explanations were considered to cause this impairment (Fig. 6). First, elevated IFP might induce changes in tumor cells, specifically by downregulating or impairing the expression of the target antigen EGFR and thereby preventing recognition by CAR-T cells. Second, the mechanical stress exerted by IFP may directly affect the structural integrity or functionality of the CAR receptor on the T cells themselves. Hence, we determined the effect of IFP on EFGR expression in PANC-1 cells in the absence of immune cells. Thus, when PANC-1 cells alone were cultured under IFP and stained for EGFR, an increased EGFR signal was observed compared with that in non-pressurized controls (Fig. 7-A,B). In BxPC-3 cell line EGFR expression levels remained unchanged upon IFP (Fig. S8). These findings suggested that the reduced cytotoxic effect of CAR-T cells under high IFP could not be attributed to downregulation or delocalization of the target antigen. In contrast, higher EGFR expression was induced under IFP. These results indicated that impaired CAR-T cell function was likely driven by pressure-induced mechanisms. EGFR expression was also compared between 2D and 3D cultures. While differences were not statistically significant, EGFR levels showed a tendency to decrease under 3D conditions, which may partially account for the delayed CAR-T cell response observed in 3D (Fig. S9).

Thus, to assess whether elevated IFP may compromise CAR-T-cell activity through functional impairment rather than through reduced antigen availability, we quantified IFN-γ secretion by CAR-T cells and control T cells under both P_0 and high-IFP conditions. Consistent with the decreased cytotoxicity observed under elevated pressure, CAR-T cells exhibited reduced IFN-γ release when exposed to high IFP (Fig. 7-C), suggesting that upon IFP, a proportion of CAR-T cells were not able to recognize tumor cells, mount a cytotoxic response and release IFN-γ [49,50]. This result was consistent with the observation that a proportion of CAR-T cells were not able to reach tumor cells (Fig. 6-A). No differences in the levels of the lymphocyte exhaustion markers PD-1, TIM-3 or LAG-3 were detected between the CAR-T cells upon IFP and P_0 conditions (Fig. S10) [51–53]. While cytokine secretion alone could not fully elucidate the underlying mechanism, these results supported the notion that pressure-induced alterations in T-cell function contributed to a diminished antitumor response. Together with the preserved and even increased EGFR expression under IFP, these findings reinforced that impaired CAR-T-cell activity arose from pressure-related functional constraints.

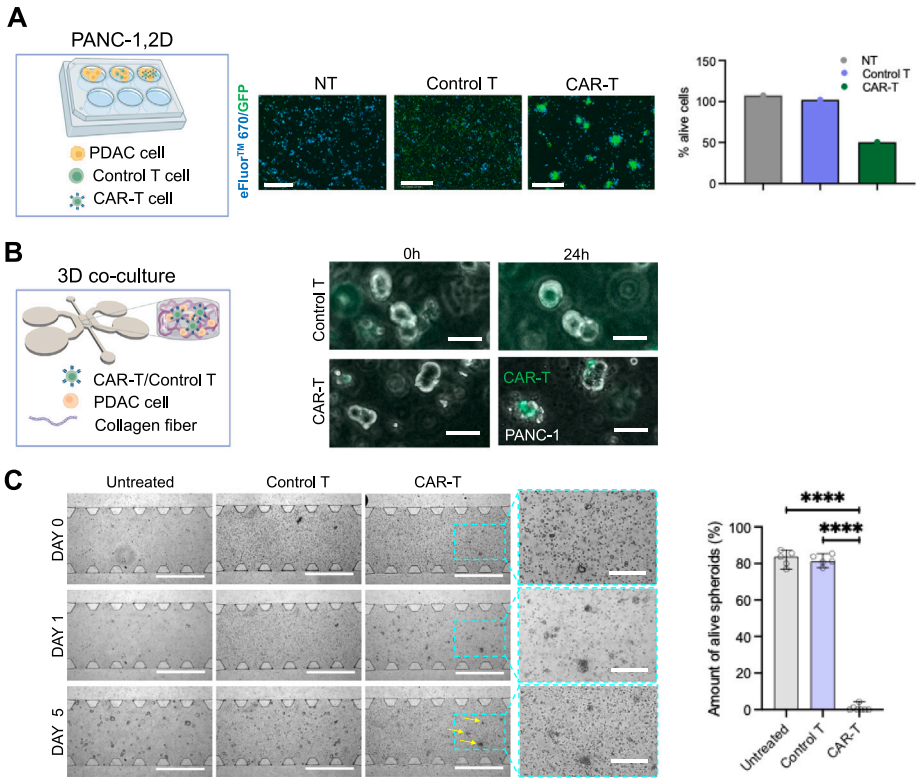

Fig. 5. Potent effectiveness of CAR-T cells against pancreatic tumor cells in 2D and 3D coculture. (A) Schematic of the experimental conditions; eFluor™ 670 and GFP images of 2D-treated PANC-1 cells with NT (nontransduced), control T (GFP+) or CAR-T (GFP+) cells (ratio 8:1) for 24 h. Scale bar, 1 mm. Quantification of eFluor™ 670 indicated approximately 50% depletion of proliferative cells upon CAR-T-cell treatment for 24 h. (B) Representative video microscopy images of 3D cocultured PANC-1 and CAR-T/Control T (GFP+) cells at 0 h and 24 h. Scale bar, 50 μm. (C) Bright field pictures of PANC-1 cells cocultured with CAR-T/control T cells at 0, 1 and 5 days after seeding. Yellow arrows highlight dead cells. A magnified image of the CAR-T cells is shown on the right. Scale bars, 1 mm and 200 μm. Percentages of PANC-1 live spheroids under untreated, control and CAR-T-cell conditions. n = 5–7 devices/condition. One-way ANOVA test was performed. Not significant when comparing Untreated vs. Control T. **** $p \leq 0.0001$. (For interpretation of the references to color in this figure legend, the reader is referred to the web version of this article.)

4. Discussion

Whereas many studies have analyzed the role of the ECM in PDAC [54,55], less attention has been given to the importance of IFP in sustaining tumor growth and resistance to therapies, which is largely due to the difficulties of analyzing this parameter noninvasively. Nonetheless, recent progress in imaging methods such as dynamic contrast-enhanced magnetic resonance imaging and elastography has facilitated a more detailed assessment of the biomechanical surroundings of tumors [56]. The PDAC IFP in patients is approximately 20 mmHg [20], whereas in normal tissues, IFP is generally around atmospheric pressure (P_0) [9,10]. Understanding the impact of IFP on tumor progression and on therapeutic delivery is key.

During the past five decades, it has been widely demonstrated that the microenvironment of solid tumors is better recreated in 3D cultures than in 2D cultures. Compared with cells grown in a 2D monolayer, 3D-cultured cells are more resistant to chemotherapy [57–59]. In this study, we developed an innovative 3D engineered PDAC-on-a-chip model with an IFP component that allowed us to analyze the role of the IFP in tumor growth and serves as a preclinical platform for testing new therapies for PDAC and other solid tumors. We constructed a 3D structure in which a microfluidic device was inserted and IFP was applied to the central chamber, where the TME is located, by means of pressure height (Fig. 2). Fiber organization in acellular collagen I hydrogels was evaluated to determine the specific impact of IFP on the matrix architecture. Under these conditions, collagen fibers remained apparently unaltered upon IFP exposure (Fig. S2), in agreement with previous observations [60]. Therefore, the observed biological effects can be attributed to the influence of pressure on cellular components rather than to mechanical alterations of the ECM.

We used two PDAC cell lines, which represent a model of the human epithelial phenotype (BxPC-3) and an intermediate epithelial–mesenchymal phenotype (PANC-1) [61], and they have different KRAS genetic signatures, a relevant gene involved in PDAC progression. BxPC-3 cells present wild-type KRAS, whereas PANC-1 cells contain a G12C mutation that results in its constitutive activation. This distinction is of vital importance since 95% of primary pancreatic tumors have mutations in the KRAS gene [62]. In addition, both cell lines express EGFR [63–65]. We observed that in both cell lines, high IFP enhanced their growth when tumors started as single-cell spheroids (and intermediate pressure affected BxPC-3 growth). However, in the case of preformed nondissociated spheroids, no evident effect of IFP was observed, suggesting that the influence of IFP might be more pronounced during the initial stages of spheroid formation than once compact structures were already established (Fig. 3). This effect on cell growth upon IFP has been previously observed *in vitro* in other tumors, such as oral squamous cell carcinoma [66].

Cells experience and sense deformation by endogenous or exogenous forces, affecting two main types of interactions, cell–ECM and cell–cell, which are internally transduced by specific mechano-signaling pathways that regulate cell lineage commitment and maintenance, survival, proliferation and specific tissue–cell function. Mechanical properties of the environment affect cell cycle progression because of the interactions between cells and the cell matrix [67,68]. Here, we observed that the proliferation rate of PANC-1 cells was enhanced upon IFP, suggesting that IFP directly affected cell cycle mechanisms (Fig. 4-A). IFP is characteristic of aggressive pancreatic tumors, and *in*

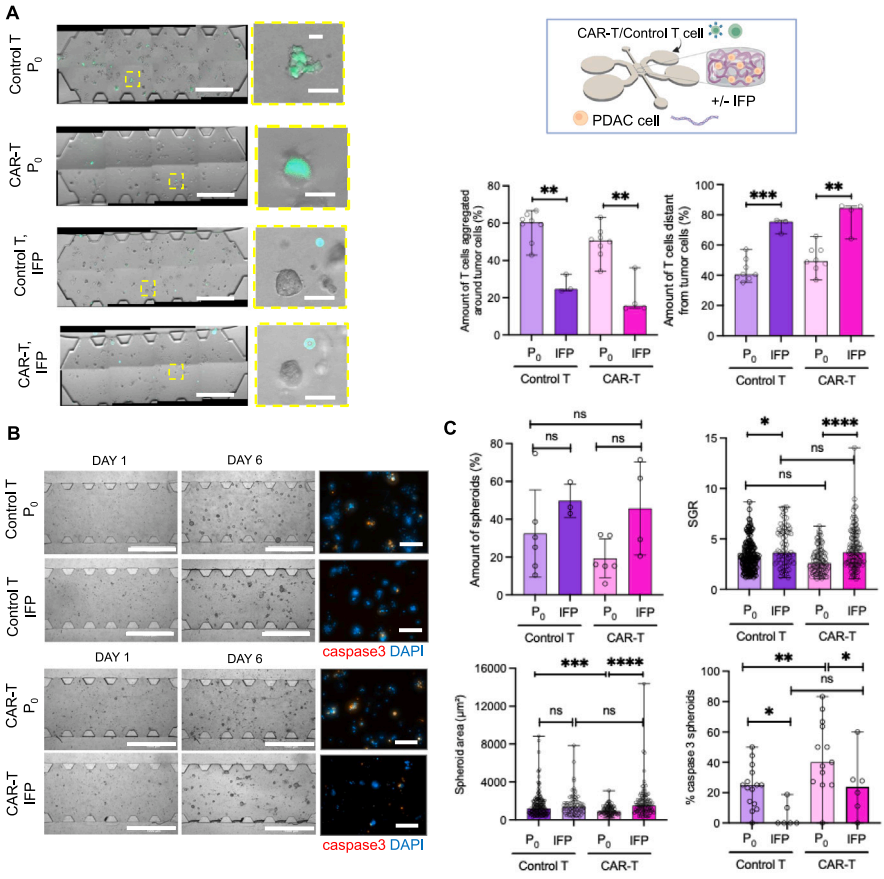

Fig. 6. CAR-T-cell therapy efficacy decreases under IFP conditions. (A) Representative images of embedded PANC-1 cells with the addition of control T or CAR-T cells through lateral channels (GFP tagged in green) with/without IFP. Scale bars: 1 mm and 100 μm (left). Percentage of lymphocytes aggregated around PANC-1 cells in control T and CAR-T conditions with/without IFP and percentage of lymphocytes distant ≥20 μm from PANC-1 cells. n = 3–5 devices/condition (right). Mann–Whitney test was performed comparing in Control T condition P_0 vs. IFP and in CAR-T condition P_0 vs. IFP. ** $p \leq 0.01$ or *** $p \leq 0.001$ when comparing P_0 and IFP conditions in both cases. (B) Representative images of PANC-1 death by caspase-3 staining (red) and DAPI (blue). Scale bars: 1 mm and 200 μm. (C) Quantification of the number of spheroids, spheroid area, SGR and percentage of caspase 3-positive cells at the end of the experiment in control T/CAR-T cells with/without IFP, n = 6-8 devices/condition. For all quantifications, one-way ANOVA test was used. ns: not significant, * $p \leq 0.05$, **$p \leq 0.01$, ***$p \leq 0.001$ and ****$p \leq 0.0001$. (For interpretation of the references to color in this figure legend, the reader is referred to the web version of this article.)

silico models have probed the association between high IFP and PDAC metastatic potential [69]. These findings align with clinical observations reporting that tumors with elevated IFP levels tend to exhibit increased metastatic behavior. Additionally, in breast cancer cells, interstitial flow increases the migration of tumor cells [70]. Surprisingly, we observed decreased actin remodeling upon IFP in our model (Fig. 4-B), which could suggest a reduced migratory capacity of these cells. This phenomenon might be explained by the application of static fluid pressure, and the absence of flow result in distinct mechanobiological mechanisms in both scenarios. Given that our goal was to study the effect of IFP on primary tumors, our model could faithfully reproduce this feature.

CAR-T cell therapy has demonstrated significant success in blood cancers [26,29,71]. However, its efficacy in solid tumors has been constrained by various factors, such as antigenic diversity and the immunosuppressive characteristics of the TME [31,72]. Additionally, inadequate biological data are available to assess critical therapeutic components. Essential information about CAR-T cell infiltration, their phenotype, and their interactions with the TME is predominantly absent, as post-infusion biopsy data are needed.

Despite some promising indications, the results from clinical trials thus far have been unsatisfactory. Multiple early-phase clinical trials using CAR-T-cell therapy for pancreatic tumors are being developed with the hope of reducing PDAC burden mortality (clinicaltrials.org) [32]. Hence, to date, limited clinical success has been obtained [73].

EGFR is a tyrosine kinase receptor (TKR) that is involved in various biological processes, including cell growth, differentiation and movement, in both normal and disease states. The hallmark of various epithelial cancers, including pancreatic cancer, is the overexpression and/or hyperactivation of EGFR, making it a target for cancer therapy [26]. A phase I clinical trial of patients with metastatic PDAC with anti-EGFR chimeric antigen receptor-modified T (CAR-T-EGFR) cells was performed. The treatment was demonstrated to be safe and partially effective in these patients [74]. Here, we studied the efficacy of our CAR-T cells directed against the EGFR family in PDAC tumors under both 2D and 3D conditions first under atmospheric pressure conditions. In 2D conditions, half of the tumor cells were targeted by CAR-T cells within 24 h (Fig. 5-A). In a 3D collagen matrix coculture, we observed the same cytotoxic effect, and after 6 days, no live spheroids were observed. This finding revealed the efficacy of CAR-T cells when they were already in the TME, where CAR-T cells were not required to penetrate a physical barrier and were not subjected to other mechanical forces, such as IFP. However, the effect of CAR-T-cell therapy was diminished when lymphocytes had to infiltrate the collagen matrix (Fig. 6-A). In this last set up, a proportion of CAR-T cells and control T cells were able to reach the TME, but the cytotoxic capacity of CAR-T cells was lower than that in the coculture scenario (Fig. 5). These findings were consistent with those of previous works indicating that low CAR-T-cell infiltration was among the main causes of the limited efficacy of this therapy in solid tumors [31,75]

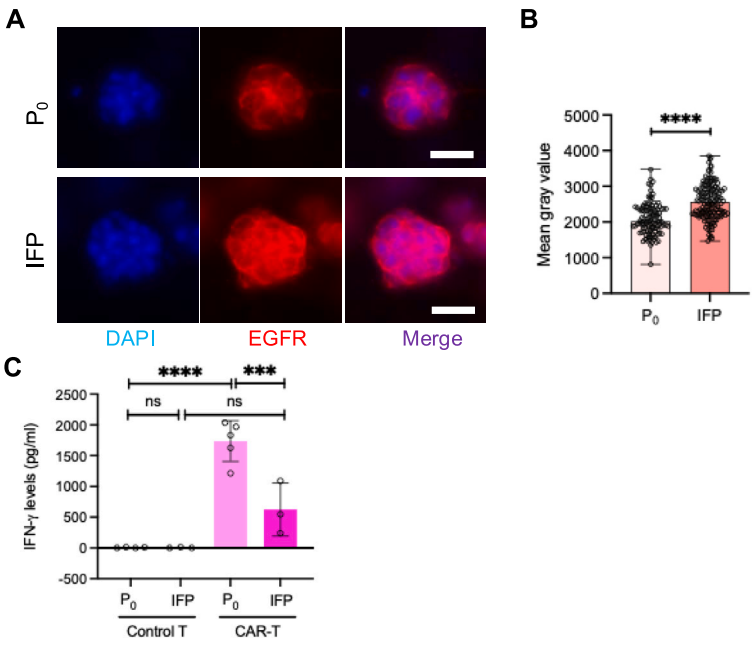

Fig. 7. IFP induces EGFR expression in PANC-1 spheroids. (A) Representative fluorescence images of samples at the end of the culture with/without high IFP. Scale bar, 50 μm. (B) Quantification of EGFR expression; n = 3 devices/condition. Unpaired t-test was performed between P_0 and IFP condition with **** $p \leq 0.0001$. (C) Quantification of IFN-γ levels in the supernatants of control T or CAR-T cells cocultured in microfluidic devices with PANC-1 cells with/without high IFP. n = 3–5 devices/condition. One-way ANOVA test was performed. ns: not sigificant, *** $p \leq 0.001$ and **** $p \leq 0.0001$.

Since it was previously observed in the laboratory that CAR-T cell speed was decreased by mechanical constraints in a microchannel-designed microfluidic device [27], we analyzed the infiltration capacity of CAR-T cells compared with that of control T cells in our device. We used CXCL12 to induce lymphocyte chemotaxis and infiltration into the collagen hydrogel, which is known to lead to lymphocyte migration to specific tissues [76] and is frequently found in the TME [45,77,78]. No measurable differences in infiltration capacity were detected between CAR-T cells and control T cells under IFP (0.3% and 0.27%, respectively) or between IFP and P_0 conditions (0.3% vs. 0.4%). While our platform did not support high-resolution temporal tracking of infiltration, the endpoint analysis suggested similar infiltration across conditions.

Phenotypic changes in immune cells can also be caused by mechanical cues, including the modulation of surface antigen expression (such as that of EGFR), the secretion of immunosuppressive cytokines, or the activation of signaling pathways that promote immune evasion. For instance, increased ECM stiffness and pressure can upregulate the expression of inhibitory checkpoint molecules or downregulate the expression of activation markers on T cells, potentially reducing CAR-T cell efficacy [79]. Moreover, recent studies have suggested that mechanical stress can directly impair immune function. For example, pressure increases PD-L1 expression in A549 lung adenocarcinoma cells and causes resistance to anti-ROR1 CAR-T cell mediated cytotoxicity [80]. For CAR-T cells, such mechanical constraints may disrupt synapse formation or interfere with downstream signaling from chimeric receptors, reducing cytokine production, granzyme release, and cell killing efficiency. Understanding the impact of IFP on CAR-T cell activity is therefore crucial for optimizing therapeutic strategies and improving treatment outcomes in patients with PDAC and other solid malignancies. In addition, IFP is an established parameter and indicator of malignant solid tumors, the levels of which increase with tumor aggressiveness [81,82].

Additionally, mechanical stress can promote an immunosuppressive tumor phenotype through mechanotransduction pathways (e.g., YAP/TAZ and integrin signaling), leading to increased secretion of TGF-β and IL-10 and upregulation of immune checkpoint molecules such as PD-L1, further affecting CAR-T cell cytotoxicity [83,84]. These effects are consistent with the clinical outcomes of the limited success of CAR-T cell therapies in solid tumors.

To test the efficacy of CAR-T cell therapy in an advanced tumor scenario, we chose high-IFP conditions for the experiments. Under high IFP, compared with basal pressure, CAR-T mediated cytotoxicity was significantly impaired, as reflected by larger spheroid sizes and lower levels of cell death (Fig. 6-C). Our results revealed that IFP not only promoted tumor growth but also significantly limited the efficacy of CAR-T cells against PDAC progression, thus enhancing tumor resistance. No difference in infiltration capacity was detected between CAR-T cells and control T cells (Fig.S7), nor were any alterations in fiber distribution identified (Fig.S2). Thus, neither mechanical access to the tumor mass nor pressure-induced matrix remodeling appeared to be the main limiting factors. Therefore, we hypothesized that IFP altered CAR-T cell function by modulating cell signaling and antigen accessibility or inducing an immunosuppressive state. First, elevated IFP may reduce EGFR accessibility by compressing tumor spheroids and altering local cytokine gradients that are necessary for CAR-T cell activation and expansion. Second, the mechanical stress exerted by IFP may directly affect the structural integrity or functionality of the CAR receptor on the T cells themselves. The isolation of the effects of pressure on PANC-1 cells revealed that EGFR expression was induced by high IFP (Fig. 7), suggesting that the induced tumor cell proliferation observed upon IFP could be partially due to the activation of the EGFR pathway [26]. Thus, the observed reduction in CAR-T cell cytotoxicity under IFP might reflect functional impairment of CAR-T cells rather than limited infiltration or targeted antigen expression. Although no differences were observed in the expression of lymphocyte exhaustion markers in CAR-T cells under IFP, a diminished IFN-γ response was observed upon IFP, suggesting a reduced ability to kill tumor cells (Fig. 7-C). Since elevated IFP is a common feature across many solid tumors, our results may provide relevant insights beyond PDAC [56]. While solid stress and IFP are related within solid tumors, their individual contributions to the TME were not investigated in this study. Thus, our findings specifically address the impact of IFP on TME, and we acknowledge that the distinct role of solid stress remains important for future investigations.

In summary, simplified 2D cultures demonstrated the robust and specific cytotoxic activity of CAR-T cells against PDAC, confirming their therapeutic potential and validating functional CAR expression as a positive control. However, when tested in a 3D culture system, especifically under elevated IFP conditions, the therapeutic efficacy of CAR-T cells was markedly reduced. These results reflect a common challenge in solid tumor treatment, which is the failure of immunotherapies to replicate their 2D success.

This study validated the use of a 3D microfluidic platform to model PDAC behavior and immune interactions under controlled mechanical conditions, further extending the benefits of microfluidics in the field of immunotherapy [85]. Our 3D system successfully mimics key features of the TME, including spheroid formation, cell–cell interactions, and response to IFP. While this work was designed as a proof-of-concept study, it provides opportunities for further investigation. The current model focuses on a specific CAR construct targeting EGFR in PDAC tumor cell lines, but future studies could explore its applicability using CAR-T cells directed against other solid tumor antigens, such as HER2, or in different tumoral tissues, such as the breast or lung. Expanding the platform in this way would help evaluate its broader relevance and reproducibility. Nonetheless, the presented microfluidic study provides a robust and physiologically relevant tool to dissect the influence of IFP on immunotherapeutic efficacy, a factor that is often ignored. Notably, while the mechanical influence of elevated IFP was isolated herein, other factors, such as cell aggregation dynamics and peripheral barrier formation, may also impact drug resistance in solid tumors and warrant dedicated future investigation. In this context, our study provides a proof-of-concept model for determining the specific influence of IFP on CAR-T-cell activity in solid tumors, offering new insights into the role of this mechanical barrier in immunotherapy development. Therapeutic strategies for patients may consider reducing IFP prior to treatment to achieve optimized success [86].

5. Conclusions

In this study, we present a PDAC-on-a-chip model that serves as a valuable preclinical platform to investigate the efficacy of immunotherapies under pathological conditions. Our findings demonstrate that IFP, a hallmark of the pancreatic TME, promotes tumor progression by enhancing proliferation and modulating cytoskeletal organization. CAR-T cells engineered to target EGFR effectively eliminated pancreatic tumor cells in both the 2D and 3D coculture systems and showed infiltration capacity comparable to that of control T cells within the 3D collagen matrix. However, the therapeutic efficacy of CAR-T cells was significantly impaired under elevated IFP, highlighting the critical role of mechanical and physical barriers in limiting immune cell function in solid tumors. This work underscores the importance of integrating biomechanical factors into immunotherapy testing platforms and supports the development of strategies to overcome TME resistance to enhance CAR-T-cell performance in solid tumors such as PDAC.

CRediT authorship contribution statement

Pilar Alamán-Díez: Writing – review & editing, Writing – original draft, Software, Investigation, Formal analysis. **Silvia Ferrer-Royo:** Writing – original draft, Investigation, Formal analysis. **Carmen Oñate Salafranca:** Writing – original draft, Investigation, Formal analysis. **Pablo Martín Compaired:** Writing – review & editing, Software, Conceptualization. **Patricia Balsas:** Writing – review & editing, Investigation, Formal analysis. **Julián Pardo:** Writing – review & editing, Supervision, Resources. **José Manuel García-Aznar:** Writing – review & editing, Supervision, Funding acquisition, Conceptualization. **Alejandra González-Loyola:** Writing – review & editing, Writing – original draft, Supervision, Methodology, Investigation, Formal analysis, Data curation, Conceptualization.

Declaration of competing interest

The authors declare that they have no known competing financial interests or personal relationships that could have appeared to influence the work reported in this paper.

Acknowledgments

This work is part of a project that has received funding from the European Research Council (ERC) under the European Union Horizon 2020 Research and Innovation Programme (ICoMICS grant agreement No. 101018587, J.M.G.A.). This publication is part of the R&D project PID2024-155384OB-C21 funded by MICIU/AEI/10.13039/501100011033 and by ERDF/EU, granted to J.M.G.A. and A.G.L., and by the Aragonese Agency Foundation for Research and Development (ARAID; A.G.L., ARAID 24/01_P) and L'Oreal–UNESCO for Women in Science 2024 (A.G.L.). S.F.R. was supported by the Fellowship and Grants Program of the Aragon Institute of Engineering Research (I3A), and C.O.S. was supported by the Agencia Estatal de Investigación (PTA2020-018510-I). P.M.C. acknowledges support from the Spanish Government through the Plan de Recuperación, Transformación y Resiliencia, and from the European Union through NextGenerationEU (Programa Investigo 076-16). Work in the J.P. laboratory is funded by FEDER (Fondo Europeo de Desarrollo Regional, Gobierno de Aragón, Group B29_23R), Grant PID2024-157582OB-I00 from the Spanish State Agency of Research, CIBER–Consorcio Centro de Investigación Biomédica en Red (CIBERINFEC, CB21/13/00087), FORTALECE, CERTERA and TERAV+ (Instituto de Salud Carlos III, ISCIII), and Grant PTA2020-018510 funded by MCIN/AEI. A.G.L. was supported by a María Zambrano Fellowship from the Spanish Ministry of Universities (Funding Programme for the attraction of international talent to the Spanish academic system) and by Instituto de Salud Carlos III (ISCIII; IHMC2200004), financed by the European Union–NextGenerationEU (LYMPDAC). We thank María Ángeles Pérez for her advice on the design of the new 3D-printed model presented in this work.

Appendix A. Supplementary data

Supplementary material related to this article can be found online at https://doi.org/10.1016/j.actbio.2026.01.050.

Data availability

Data will be shared by the corresponding author upon request.

References

[1] P. Rawla, T. Sunkara, V. Gaduputi, Epidemiology of pancreatic cancer: global trends, etiology and risk factors, World J. Oncol. 10 (1) (2019) 10, http://dx.doi.org/10.14740/wjon1166.

[2] L. Rahib, B.D. Smith, R. Aizenberg, A.B. Rosenzweig, J.M. Fleshman, L.M. Matrisian, Projecting cancer incidence and deaths to 2030: the unexpected burden of thyroid, liver, and pancreas cancers in the United States, Cancer Res. 74 (11) (2014) 2913–2921, http://dx.doi.org/10.1158/0008-5472.CAN-14-0155.

[3] W.J. Ho, E.M. Jaffee, L. Zheng, The tumour microenvironment in pancreatic cancer—clinical challenges and opportunities, Nat. Rev. Clin. Oncol. 17 (9) (2020) 527–540, http://dx.doi.org/10.1038/s41571-020-0363-5.

[4] X. Zhao, Z. Li, Z. Gu, A new era: tumor microenvironment in chemoresistance of pancreatic cancer, J. Cancer Sci. Clin. Ther. 6 (1) (2022) 61, http://dx.doi.org/10.26502/jcsct.5079146.

[5] M. Caban, E. Małecka-Wojciesko, Gaps and opportunities in the diagnosis and treatment of pancreatic cancer, Cancers 15 (23) (2023) 5577, http://dx.doi.org/10.3390/CANCERS15235577.

[6] Y. Jiang, D.P. Sohal, Pancreatic adenocarcinoma management, JCO Oncol. Pract. 19 (1) (2023) 19–32, http://dx.doi.org/10.1200/OP.22.00328.

[7] T. Stylianopoulos, L.L. Munn, R.K. Jain, Reengineering the physical microenvironment of tumors to improve drug delivery and efficacy: from mathematical modeling to bench to bedside, Trends Cancer 4 (4) (2018) 292–319, http://dx.doi.org/10.1016/j.trecan.2018.02.005.

[8] B. Blanco, H. Gomez, J. Melchor, R. Palma, J. Soler, G. Rus, Mechanotransduction in tumor dynamics modeling, Phys. Life Rev. 44 (2023) 279–301, http://dx.doi.org/10.1016/j.plrev.2023.01.017.

[9] J. Kopecka, I.C. Salaroglio, E. Perez-Ruiz, A.B. Sarmento-Ribeiro, S. Saponara, J. De Las Rivas, C. Riganti, Hypoxia as a driver of resistance to immunotherapy, Drug Resist. Updates 59 (2021) 100787, http://dx.doi.org/10.1016/j.drup.2021.100787.

[10] M. Orth, P. Metzger, S. Gerum, J. Mayerle, G. Schneider, C. Belka, M. Schnurr, K. Lauber, Pancreatic ductal adenocarcinoma: biological hallmarks, current status, and future perspectives of combined modality treatment approaches, Radiat. Oncol. 14 (1) (2019) 1–20, http://dx.doi.org/10.1186/s13014-019-1345-6.

[11] P.P. Provenzano, C. Cuevas, A.E. Chang, V.K. Goel, D.D. Von Hoff, S.R. Hingorani, Enzymatic targeting of the stroma ablates physical barriers to treatment of pancreatic ductal adenocarcinoma, Cancer Cell 21 (3) (2012) 418–429, http://dx.doi.org/10.1016/j.ccr.2012.01.007.

[12] C.C. DuFort, K.E. DelGiorno, M.A. Carlson, R.J. Osgood, C. Zhao, Z. Huang, C.B. Thompson, R.J. Connor, C.D. Thanos, J.S. Brockenbrough, et al., Interstitial pressure in pancreatic ductal adenocarcinoma is dominated by a gel-fluid phase, Biophys. J. 110 (9) (2016) 2106–2119, http://dx.doi.org/10.1016/j.bpj.2016.03.040.

[13] H. Peng, Z. Chao, Z. Wang, X. Hao, Z. Xi, S. Ma, X. Guo, J. Zhang, Q. Zhou, G. Qu, et al., Biomechanics in the tumor microenvironment: from biological functions to potential clinical applications, Exp. Hematol. Oncol. 14 (1) (2025) 4, http://dx.doi.org/10.1186/s40164-024-00591-7.

[14] G. Helmlinger, P.A. Netti, H.C. Lichtenbeld, R.J. Melder, R.K. Jain, Solid stress inhibits the growth of multicellular tumor spheroids, Nature Biotechnol. 15 (8) (1997) 778–783, http://dx.doi.org/10.1038/nbt0897-778.

[15] G. Cheng, J. Tse, R.K. Jain, L.L. Munn, Micro-environmental mechanical stress controls tumor spheroid size and morphology by suppressing proliferation and inducing apoptosis in cancer cells, PLoS One 4 (2) (2009) e4632, http://dx.doi.org/10.1371/journal.pone.0004632.

[16] F. Montel, M. Delarue, J. Elgeti, D. Vignjevic, G. Cappello, J. Prost, Isotropic stress reduces cell proliferation in tumor spheroids, New J. Phys. 14 (5) (2012) 055008, http://dx.doi.org/10.1088/1367-2630/14/5/055008.

[17] M. Delarue, F. Montel, D. Vignjevic, J. Prost, J.-F. Joanny, G. Cappello, Compressive stress inhibits proliferation in tumor spheroids through a volume limitation, Biophys. J. 107 (8) (2014) 1821–1828, http://dx.doi.org/10.1016/j.bpj.2014.08.031.

[18] P. Van Liedekerke, J. Neitsch, T. Johann, K. Alessandri, P. Nassoy, D. Drasdo, Quantitative cell-based model predicts mechanical stress response of growing tumor spheroids over various growth conditions and cell lines, PLoS Comput. Biol. 15 (3) (2019) e1006273, http://dx.doi.org/10.1371/journal.pcbi.1006273.

[19] I.G. Gonçalves, J.M. Garcia-Aznar, Extracellular matrix density regulates the formation of tumour spheroids through cell migration, PLoS Comput. Biol. 17 (2) (2021) e1008764, http://dx.doi.org/10.1371/journal.pcbi.1008764.

[20] V.P. Chauhan, Y. Boucher, C.R. Ferrone, S. Roberge, J.D. Martin, T. Stylianopoulos, N. Bardeesy, R.A. DePinho, T.P. Padera, L.L. Munn, et al., Compression of pancreatic tumor blood vessels by hyaluronan is caused by solid stress and not interstitial fluid pressure, Cancer Cell 26 (1) (2014) 14–15, http://dx.doi.org/10.1016/j.ccr.2014.06.003.

[21] L.M.K. Hansem, R. Huang, C.S. Wegner, T.G. Simonsen, J.-V. Gaustad, A. Hauge, E.K. Rofstad, Intratumor heterogeneity in interstitial fluid pressure in cervical and pancreatic carcinoma xenografts, Transl. Oncol. 12 (8) (2019) 1079–1085, http://dx.doi.org/10.1016/j.tranon.2019.05.012.

[22] M. Shang, S.B. Lim, K. Jiang, Y.S. Yap, B.L. Khoo, J. Han, C.T. Lim, Microfluidic studies of hydrostatic pressure-enhanced doxorubicin resistance in human breast cancer cells, Lab Chip 21 (4) (2021) 746–754, http://dx.doi.org/10.1039/D0LC01103G.

[23] B.C. Özdemir, T. Pentcheva-Hoang, J.L. Carstens, X. Zheng, C.-C. Wu, T.R. Simpson, H. Laklai, H. Sugimoto, C. Kahlert, S.V. Novitskiy, et al., Depletion of carcinoma-associated fibroblasts and fibrosis induces immunosuppression and accelerates pancreas cancer with reduced survival, Cancer Cell 25 (6) (2014) 719–734, http://dx.doi.org/10.1016/j.ccr.2014.04.005.

[24] A.N. Hosein, S.K. Dougan, A.J. Aguirre, A. Maitra, Translational advances in pancreatic ductal adenocarcinoma therapy, Nat. Cancer 3 (3) (2022) 272–286, http://dx.doi.org/10.1038/s43018-022-00349-2.

[25] R.K. Ramanathan, S.L. McDonough, P.A. Philip, S.R. Hingorani, J. Lacy, J.S. Kortmansky, J. Thumar, E.G. Chiorean, A.F. Shields, D. Behl, et al., Phase IB/II randomized study of FOLFIRINOX plus pegylated recombinant human hyaluronidase versus FOLFIRINOX alone in patients with metastatic pancreatic adenocarcinoma: SWOG S1313, J. Clin. Oncol. 37 (13) (2019) 1062–1069, http://dx.doi.org/10.1200/JCO.18.01295.

[26] R.C. Sterner, R.M. Sterner, CAR-T cell therapy: current limitations and potential strategies, Blood Cancer J. 11 (4) (2021) http://dx.doi.org/10.1038/s41408-021-00459-7.

[27] J. Zhang-Zhou, N.M. Meno, C.O. Salafranca, M.J. Gomez-Benito, P.E. Guerrero, J.P. Jimeno, J.M. García-Aznar, CAR-T cells are more affected than T lymphocytes by mechanical constraints: A microfluidic-based approach, Life Sci. 363 (2025) 123335, http://dx.doi.org/10.1016/j.lfs.2024.123335.

[28] K. Fujiwara, A. Tsunei, H. Kusabuka, E. Ogaki, M. Tachibana, Antigen receptor regulate receptor expression and, Cells (2020) http://dx.doi.org/10.3390/cells9051182.

[29] I. Scarfò, M.V. Maus, Current approaches to increase CAR T cell potency in solid tumors: Targeting the tumor microenvironment, J. ImmunoTher. Cancer 5 (1) (2017) 1–8, http://dx.doi.org/10.1186/s40425-017-0230-9.

[30] F. Marofi, R. Motavalli, V.A. Safonov, L. Thangavelu, A.V. Yumashev, M. Alexander, N. Shomali, M.S. Chartrand, Y. Pathak, M. Jarahian, S. Izadi, A. Hassanzadeh, N. Shirafkan, S. Tahmasebi, F.M. Khiavi, CAR T cells in solid tumors: challenges and opportunities, Stem Cell Res. Ther. 12 (1) (2021) 1–16, http://dx.doi.org/10.1186/s13287-020-02128-1.

[31] C. Zhu, Q. Wu, T. Sheng, J. Shi, X. Shen, J. Yu, Y. Du, J. Sun, T. Liang, K. He, Y. Ding, H. Li, Z. Gu, W. Wang, Rationally designed approaches to augment CAR-T therapy for solid tumor treatment, Bioact. Mater. 33 (November 2023) (2024) 377–395, http://dx.doi.org/10.1016/j.bioactmat.2023.11.002.

[32] A. Czaplicka, M. Lachota, L. Pączek, R. Zagożdżon, B. Kaleta, Chimeric antigen receptor T cell therapy for pancreatic cancer: A review of current evidence, Cells 13 (1) (2024) http://dx.doi.org/10.3390/cells13010101.

[33] M. Wehrli, S. Guinn, F. Birocchi, A. Kuo, Y. Sun, R.C. Larson, A.J. Almazan, I. Scarfò, A.A. Bouffard, S.R. Bailey, et al., Mesothelin CAR T cells secreting anti-FAP/anti-CD3 molecules efficiently target pancreatic adenocarcinoma and its stroma, Clin. Cancer Res. 30 (9) (2024) 1859–1877, http://dx.doi.org/10.1158/1078-0432.CCR-23-3841.

[34] H.K. Lin, D.A. Blake, T. Liu, R. Freeman, G.B. Lesinski, L. Yang, S. Rafiq, Muc16CD is a novel CAR T cell target antigen for the treatment of pancreatic cancer, Mol. Ther.: Oncol. 32 (December) (2024) 200868, http://dx.doi.org/10.1016/j.omton.2024.200868.

[35] V. Wang, M. Gauthier, V. Decot, L. Reppel, D. Bensoussan, Systematic review on CAR-T cell clinical trials up to 2022: Academic center input, Cancers 15 (4) (2023) http://dx.doi.org/10.3390/cancers15041003.

[36] D.M. Davies, J. Foster, S.J. Van Der Stegen, A.C. Parente-Pereira, L. Chiapero-Stanke, G.J. Delinassios, S.E. Burbridge, V. Kao, Z. Liu, L. Bosshard-Carter, et al., Flexible targeting of ErbB dimers that drive tumorigenesis by using genetically engineered T cells, Mol. Med. 18 (4) (2012) 565–576, http://dx.doi.org/10.2119/molmed.2011.00493Abstract.

[37] P. Wee, Z. Wang, Epidermal growth factor receptor cell proliferation signaling pathways, Cancers 9 (5) (2017) 1–45, http://dx.doi.org/10.3390/cancers9050052.

[38] Y.C. Chen, X. Lou, Z. Zhang, P. Ingram, E. Yoon, High-Throughput cancer cell sphere formation for characterizing the efficacy of photo dynamic therapy in 3D cell cultures, Sci. Rep. 5 (December 2014) (2015) 1–12, http://dx.doi.org/10.1038/srep12175.

[39] Y. Shin, S. Han, J.S. Jeon, K. Yamamoto, I.K. Zervantonakis, R. Sudo, R.D. Kamm, S. Chung, Microfluidic assay for simultaneous culture of multiple cell types on surfaces or within hydrogels, Nat. Protoc. 7 (2012) 1247, http://dx.doi.org/10.1038/nprot.2012.051.

[40] S. Hernández-Hatibi, P.E. Guerrero, J.M. García-Aznar, E. García-Gareta, Polydopamine interfacial coating for stable tumor-on-a-chip models: application for pancreatic ductal adenocarcinoma, Biomacromolecules 25 (8) (2024) 5169–5180, http://dx.doi.org/10.1021/acs.biomac.4c00551.

[41] P. Alamán-Díez, C. Borau, P.E. Guerrero, H. Amaveda, M. Mora, J.M. Fraile, E. García-Gareta, J.M. García-Aznar, M.Á. Pérez, Collagen-laponite nanoclay hydrogels for tumor spheroid growth, Biomacromolecules 24 (6) (2023) 2879–2891, http://dx.doi.org/10.1021/acs.biomac.3c00257.

[42] J. Plou, Y. Juste-Lanas, V. Olivares, C. Del Amo, C. Borau, J. García-Aznar, From individual to collective 3D cancer dissemination: roles of collagen concentration and TGF-β, Sci. Rep. 8 (1) (2018) 12723, http://dx.doi.org/10.1038/s41598-018-30683-4.

[43] M.D. Basson, B. Zeng, C. Downey, M.P. Sirivelu, J.J. Tepe, Increased extracellular pressure stimulates tumor proliferation by a mechanosensitive calcium channel and PKC-β, Mol. Oncol. 9 (2) (2015) 513–526, http://dx.doi.org/10.1016/j.molonc.2014.10.008.

[44] P. Purkayastha, M.K. Jaiswal, T.P. Lele, Molecular cancer cell responses to solid compressive stress and interstitial fluid pressure, Cytoskeleton 78 (6) (2021) 312–322, http://dx.doi.org/10.1002/cm.21680.

[45] M.A. Morgan, A. Schambach, Engineering CAR-T cells for improved function against solid tumors, Front. Immunol. 9 (2018) 2493, http://dx.doi.org/10.3389/fimmu.2018.02493.

[46] A. Yamada, S. Kitano, M. Matsusaki, Cellular memory function from 3D to 2D: Three-dimensional high density collagen microfiber cultures induce their resistance to reactive oxygen species, Mater. Today Bio 26 (2024) 101097, http://dx.doi.org/10.1016/j.mtbio.2024.101097.

[47] J.S. Liles, J.P. Arnoletti, C.-W.D. Tzeng, J.H. Howard, A.V. Kossenkov, P. Kulesza, M.J. Heslin, A. Frolov, ErbB3 expression promotes tumorigenesis in pancreatic adenocarcinoma, Cancer Biol. Ther. 10 (6) (2010) 555–563, http://dx.doi.org/10.4161/cbt.10.6.12532.

[48] M. Zanoni, F. Piccinini, C. Arienti, A. Zamagni, S. Santi, R. Polico, A. Bevilacqua, A. Tesei, 3D tumor spheroid models for in vitro therapeutic screening: a systematic approach to enhance the biological relevance of data obtained, Sci. Rep. 6 (1) (2016) 19103, http://dx.doi.org/10.1038/srep19103.

[49] R.C. Larson, M.C. Kann, S.R. Bailey, N.J. Haradhvala, P.M. Llopis, A.A. Bouffard, I. Scarfó, M.B. Leick, K. Grauwet, T.R. Berger, et al., CAR T cell killing requires the IFNγR pathway in solid but not liquid tumours, Nature 604 (7906) (2022) 563–570, http://dx.doi.org/10.1038/s41586-022-04585-5.

[50] L. Hong, L. Ye, The interferon-γ receptor pathway: a new way to regulate CAR T cell-solid tumor cell adhesion, Signal Transduct. Target. Ther. 7 (1) (2022) 315, http://dx.doi.org/10.1038/s41392-022-01165-x.

[51] T. Kouro, H. Himuro, T. Sasada, Exhaustion of CAR T cells: potential causes and solutions, J. Transl. Med. 20 (1) (2022) 239, http://dx.doi.org/10.1186/s12967-022-03442-3.

[52] Y. Wolf, A.C. Anderson, V.K. Kuchroo, TIM3 comes of age as an inhibitory receptor, Nat. Rev. Immunol. 20 (3) (2020) 173–185, http://dx.doi.org/10.1038/s41577-019-0224-6.

[53] M. Hofmann, R. Thimme, W.W. Schamel, PD-1 and LAG-3: synergistic fostering of T cell exhaustion, Signal Transduct. Target. Ther. 9 (1) (2024) 291, http://dx.doi.org/10.1038/s41392-024-02000-1.

[54] M. Weniger, K.C. Honselmann, A.S. Liss, The extracellular matrix and pancreatic cancer: a complex relationship, Cancers 10 (9) (2018) 316, http://dx.doi.org/10.3390/cancers10090316.

[55] J. Kota, J. Hancock, J. Kwon, M. Korc, Pancreatic cancer: Stroma and its current and emerging targeted therapies, Cancer Lett. 391 (2017) 38–49, http://dx.doi.org/10.1016/j.canlet.2016.12.035.

[56] H. Salavati, C. Debbaut, P. Pullens, W. Ceelen, Interstitial fluid pressure as an emerging biomarker in solid tumors, Biochim. Biophys. Acta (BBA)-Rev. Cancer 1877 (5) (2022) 188792, http://dx.doi.org/10.1016/j.bbcan.2022.188792.

[57] H. Song, G.-h. Cai, J. Liang, D.-s. Ao, H. Wang, Z.-h. Yang, Three-dimensional culture and clinical drug responses of a highly metastatic human ovarian cancer HO-8910PM cells in nanofibrous microenvironments of three hydrogel biomaterials, J. Nanobiotechnology 18 (1) (2020) 90, http://dx.doi.org/10.1186/s12951-020-00646-x.

[58] M. Liu, X. Zhang, C. Long, H. Xu, X. Cheng, J. Chang, C. Zhang, C. Zhang, X. Wang, Collagen-based three-dimensional culture microenvironment promotes epithelial to mesenchymal transition and drug resistance of human ovarian cancer in vitro, RSC Adv. 8 (16) (2018) 8910–8919, http://dx.doi.org/10.1039/c7ra13742g.

[59] O. Firuzi, P.P. Che, B. El Hassouni, M. Buijs, S. Coppola, M. Löhr, N. Funel, R. Heuchel, I. Carnevale, T. Schmidt, et al., Role of c-MET inhibitors in overcoming drug resistance in spheroid models of primary human pancreatic cancer and stellate cells, Cancers 11 (5) (2019) 638, http://dx.doi.org/10.3390/cancers11050638.

[60] K.-W. Lee, D.B. Stolz, Y. Wang, Substantial expression of mature elastin in arterial constructs, Proc. Natl. Acad. Sci. 108 (7) (2011) 2705–2710, http://dx.doi.org/10.1073/pnas.1017834108.

[61] T. Puls, X. Tan, C.F. Whittington, S.L. Voytik-Harbin, 3D collagen fibrillar microstructure guides pancreatic cancer cell phenotype and serves as a critical design parameter for phenotypic models of EMT, PLoS One 12 (11) (2017) e0188870, http://dx.doi.org/10.1371/journal.pone.0188870.

[62] K.L. Bryant, J.D. Mancias, A.C. Kimmelman, C.J. Der, KRAS: feeding pancreatic cancer proliferation, Trends Biochem. Sci. 39 (2) (2014) 91–100, http://dx.doi.org/10.1016/j.tibs.2013.12.004.

[63] J. Lu, M.M. Yassin, Y. Guo, Y. Yang, F. Cao, J. Fang, A. Zaman, H. Hassan, X. Zeng, X. Miao, et al., Ischemic perfusion radiomics: assessing neurological impairment in acute ischemic stroke, Front. Neurol. 15 (2024) 1441055, http://dx.doi.org/10.3389/fneur.2024.1441055.

[64] J. Boonstra, P. Rijken, B. Humbel, F. Cremers, A. Verkleij, P.v.B. en Henegouwen, The epidermal growth factor, Cell Biol. Int. 19 (5) (1995) 413–430, http://dx.doi.org/10.1006/cbir.1995.1086.

[65] Y. Zhang, S. Banerjee, Z.-w. Wang, D.J. Marciniak, A.P. Majumdar, F.H. Sarkar, Epidermal growth factor receptor–related protein inhibits cell growth and induces apoptosis of BxPC3 pancreatic cancer cells, Cancer Res. 65 (9) (2005) 3877–3882, http://dx.doi.org/10.1158/0008-5472.CAN-04-3654.

[66] T. Yu, K. Liu, Y. Wu, J. Fan, J. Chen, C. Li, G. Zhu, Z. Wang, L. Li, High interstitial fluid pressure promotes tumor cell proliferation and invasion in oral squamous cell carcinoma, Int. J. Mol. Med. 32 (5) (2013) 1093–1100, http://dx.doi.org/10.3892/ijmm.2013.1496.

[67] M. Uroz, S. Wistorf, X. Serra-Picamal, V. Conte, M. Sales-Pardo, P. Roca-Cusachs, R. Guimerà, X. Trepat, Regulation of cell cycle progression by cell–cell and cell–matrix forces, Nature Cell Biol. 20 (6) (2018) 646–654, http://dx.doi.org/10.1038/s41556-018-0107-2.

[68] P.P. Provenzano, P.J. Keely, Mechanical signaling through the cytoskeleton regulates cell proliferation by coordinated focal adhesion and rho gtpase signaling, J. Cell Sci. 124 (8) (2011) 1195–1205, http://dx.doi.org/10.1242/jcs.067009.

[69] G. Naevdal, E.K. Rofstad, K. Søreide, S. Evje, Fluid-sensitive migration mechanisms predict association between metastasis and high interstitial fluid pressure in pancreatic cancer, J. Biomech. 145 (2022) 111362, http://dx.doi.org/10.1016/j.jbiomech.2022.111362.

[70] U. Haessler, J.C. Teo, D. Foretay, P. Renaud, M.A. Swartz, Migration dynamics of breast cancer cells in a tunable 3D interstitial flow chamber, Integr. Biol. 4 (4) (2012) 401–409, http://dx.doi.org/10.1039/c1ib00128k.

[71] L.L.-W. Wang, M.E. Janes, N. Kumbhojkar, N. Kapate, J.R. Clegg, S. Prakash, M.K. Heavey, Z. Zhao, A.C. Anselmo, S. Mitragotri, Cell therapies in the clinic, Bioeng. Transl. Med. 6 (2) (2021) e10214, http://dx.doi.org/10.1002/btm2.10214.

[72] A. Esmaeilzadeh, K. Hadiloo, M. Jabbari, R. Elahi, Current progress of chimeric antigen receptor (CAR) T versus CAR NK cell for immunotherapy of solid tumors, Life Sci. 337 (2024) 122381, http://dx.doi.org/10.1016/j.lfs.2023.122381.

[73] L.R.C. Barros, S.C.F. Couto, D. da Silva Santurio, E.A. Paixão, F. Cardoso, V.J. da Silva, P. Klinger, P.D.A.C. Ribeiro, F.A. Rós, T.G.M. Oliveira, E.M. Rego, R.N. Ramos, V. Rocha, Systematic review of available CAR-T cell trials around the world, Cancers 14 (11) (2022) 1–12, http://dx.doi.org/10.3390/cancers14112667.

[74] Y. Liu, Y. Guo, Z. Wu, K. Feng, C. Tong, Y. Wang, H. Dai, F. Shi, Q. Yang, W. Han, Anti-EGFR chimeric antigen receptor-modified T cells in metastatic pancreatic carcinoma: a phase I clinical trial, Cytotherapy 22 (10) (2020) 573–580, http://dx.doi.org/10.1016/j.jcyt.2020.04.088.

[75] L. Peng, G. Sferruzza, L. Yang, L. Zhou, S. Chen, CAR-T and CAR-NK as cellular cancer immunotherapy for solid tumors, Cell. Mol. Immunol. 21 (10) (2024) 1089–1108, http://dx.doi.org/10.1038/s41423-024-01207-0.

[76] M. Meiron, Y. Zohar, R. Anunu, G. Wildbaum, N. Karin, CXCL12 (SDF-1α) suppresses ongoing experimental autoimmune encephalomyelitis by selecting antigen-specific regulatory T cells, J. Exp. Med. 205 (11) (2008) 2643–2655, http://dx.doi.org/10.1084/jem.20080730.

[77] D.T. Nguyen, E. Ogando-Rivas, R. Liu, T. Wang, J. Rubin, L. Jin, H. Tao, W.W. Sawyer, H.R. Mendez-Gomez, M. Cascio, et al., CAR T cell locomotion in solid tumor microenvironment, Cells 11 (12) (2022) 1974, http://dx.doi.org/10.3390/cells11121974.

[78] U. Patel, J. Abernathy, B.N. Savani, O. Oluwole, S. Sengsayadeth, B. Dholaria, CAR T cell therapy in solid tumors: A review of current clinical trials, EJHaem 3 (2022) 24–31, http://dx.doi.org/10.1002/jha2.356.

[79] I. Klabukov, A.E. Kabakov, A. Yakimova, D. Baranovskii, D. Sosin, D. Atiakshin, M. Ignatyuk, E. Yatsenko, V. Rybachuk, E. Evstratova, et al., Tumor-associated extracellular matrix obstacles for CAR-T cell therapy: approaches to overcoming, Curr. Oncol. 32 (2) (2025) 79, http://dx.doi.org/10.3390/curroncol32020079.

[80] Z. Ou, X. Dou, N. Tang, G. Liu, Pressure increases PD-L1 expression in A549 lung adenocarcinoma cells and causes resistance to anti-ROR1 CAR T cell-mediated cytotoxicity, Sci. Rep. 12 (1) (2022) 6919, http://dx.doi.org/10.1038/s41598-022-10905-6.

[81] C.C. DuFort, K.E. DelGiorno, S.R. Hingorani, Mounting pressure in the microenvironment: fluids, solids, and cells in pancreatic ductal adenocarcinoma, Gastroenterology 150 (7) (2016) 1545–1557, http://dx.doi.org/10.1053/j.gastro.2016.03.040.

[82] S. Ferretti, P.R. Allegrini, M.M. Becquet, P.M. McSheehy, Tumor interstitial fluid pressure as an early-response marker for anticancer therapeutics, Neoplasia 11 (9) (2009) 874–881, http://dx.doi.org/10.1593/neo.09554.

[83] M.W. Pickup, J.K. Mouw, V.M. Weaver, The extracellular matrix modulates the hallmarks of cancer, EMBO Rep. 15 (12) (2014) 1243–1253, http://dx.doi.org/10.15252/embr.201439246.

[84] M. Kalli, T. Stylianopoulos, Defining the role of solid stress and matrix stiffness in cancer cell proliferation and metastasis, Front. Oncol. 8 (2018) 55, http://dx.doi.org/10.3389/fonc.2018.00055.

[85] H.W. Hou, A.J. Chung, C.T. Lim, Microfluidics and nanofluidics for immunotherapy, Biomicrofluidics 19 (4) (2025) http://dx.doi.org/10.1063/5.0281840.

[86] S.J. Lunt, A. Fyles, R.P. Hill, M. Milosevic, Interstitial fluid pressure in tumors: therapeutic barrier and biomarker of angiogenesis, Future Oncol. 4 (6) (2008) 793–802, http://dx.doi.org/10.2217/14796694.4.6.793.